Supporting Information for "Lagrangian Timescales of Southern Ocean Upwelling in a Hierarchy of Model Resolutions"

Henri F. Drake,[1,2] Adele K. Morrison,[1,3] Stephen M. Griffies,[1,4] Jorge L. Sarmiento,[1] Wilbert Weijer,[5] Alison R. Gray[1,6]

Contents of this file

1. Text S1 to S4

2. Figures S1 to S7

Additional Supporting Information (Files uploaded separately)

1. Captions for Movie S1

Introduction

The supplementary information provided here serves two purposes: firstly, we provide additional useful figures and a movie; secondly, we provide supporting text regarding: spectral analysis in support of our hypothesis that temporally degrading velocity fields corresponds to removing eddy energy in a comparable way to degrading horizontal resolution (Text S1); sensitivity of our results to the definition of the upper ocean (Text S2);

Corresponding author: Henri F. Drake, Massachusetts Institute of Technology, 77 Massachusetts Ave., Cambridge, MA 02139, USA. (hdrake@mit.edu)

[1]Department of Atmospheric and Oceanic

potential sources of error in the calculation of Lagrangian Upwelling Transport (Text S3);

the inverse Gaussian fits to the transit time distributions (Text S4).

Sciences, Princeton University, Princeton, New Jersey, USA.

[2]Currently at Research School of Earth Sciences, Australian National University, Canberra, Australian Capital Territory, Australia

[3]Currently at Massachusetts Institute of Technology and Woods Hole Oceanographic Institution Joint Program in Oceanography, MA, USA.

[4]NOAA/Geophysical Fluid Dynamics Laboratory, Princeton, New Jersey, USA.

[5]Los Alamos National Laboratory, Los Alamos, New Mexico, USA.

[6]Currently at School of Oceanography, University of Washington, Seattle, Washington, USA.

Text S1. In the main text, we hypothesized that the temporal degradation of CM2.6 velocity output from 5-day averages to monthly averages removes eddy kinetic energy at all scales, but the energetic mesoscale in particular. We begin by calculating the eddy velocities (and subsequently eddy kinetic energy) by removing the 1-year mean from the velocity output. Using code from *Rocha et al.* [2016] (python package pyspec available at https://github.com/pyspec/pyspec), we compute the wavenumber spectra of horizontal and vertical eddy kinetic energy (removing the spatial mean eddy kinetic energy and detrending in both the zonal and meridional directions) over a region at 1000 meters depth from 155°W to 135°W, 60°S to 52°S (Supplementary Fig. S2a,b). *Tamsitt et al.* [2017] found enhanced Lagrangian upwelling in this region of high eddy kinetic energy where the ACC intersects the Pacific-Antarctic Ridge. Isotropic spectra are computed from zonal-meridional spectra by interpolating to polar coordinates and selecting only the radial component (Supplementary Fig. S2c,d). We compute the spectra of each snapshot (5-day or monthly averages, depending on the experiment) in the first year of output and calculate the mean (solid lines) and spread (shaded regions, to give a sense of the variability). The similarity between the zonal, meridional, and isotropic wavenumber spectra for the vertical eddy kinetic energy suggests that the turbulence is relatively isotropic at these length scales. Focusing now on the isotropic wavenumber spectra for vertical eddy kinetic energy (panel (c)), we note that CM2.5-5day has over an order of magnitude less vertical eddy kinetic energy than CM2.6-5day at all resolved scales (and zero energy at smaller unresolved scales). The red line shows that temporal degradation of CM2.6-5day removes vertical eddy kinetic energy at all spatial scales and causes its spectra

to resemble that of CM2.5-5day (although it still contains some energy at scales unresolved in CM2.5-5day). Panel (d) shows the isotropic wavenumber spectrum of horizontal eddy kinetic energy, which has a steeper slope at small scales than the vertical eddy kinetic energy. We note that for the horizontal eddy kinetic energy spectrum, the difference between CM2.5-5day and CM2.6-monthly is less significant, but increases towards smaller scales. This analysis was repeated for several other regions of the Antarctic Circumpolar Current and the qualitative conclusions above are unchanged therein (not shown).

Text S2. In the paper, we define the upper ocean as the part of the ocean shallower than 300 m. Here, we show that the results of the paper are robust by exploring other definitions for the upper ocean. In Supplementary Figure S3a-e, we plot versions of Figure 2a that show the Transit-Time Distributions (TTD) for particle-transport to travel from depth at 30°S to the upper ocean, where we vary the depth of the base of the upper ocean. The trend of shorter timescale when resolution is refined is shown for all definitions of the upper ocean, except perhaps the 900 m definition, which is quite close to the upper limit of the release depths of 1000-4000 m.

In Supplementary Figure S3f, we define the upper ocean as the surface mixed layer, as defined by the 0.03 kg/m^2 threshold definition used in the ocean models. For each model grid column, 5-day averaged mixed layer depths of the nearest grid-point are linearly interpolated in time and compared to particle depth sampled every 5 days. Qualitatively similar results are found with the constant 300 m depth definition. We note that we prefer the 300 m depth definition because it is constant across all experiments, whereas differences in the spatio-temporal distributions of mixed-layer depths across the exper-

iments make it difficult to know whether any differences in the timescale are due to enhanced vertical motion or lateral advection across a sloped mixed layer base. Indeed, in CM2-1deg-5day and CM2.6-monthly, the mixed-layer definition of the upper ocean causes enough particle-transport (10% total transport) to be laterally advected into deep mid-latitude mixed layers (500-800 m deep) to skew the TTD towards shorter timescales (Supplementary Fig. S6, S7). We note that in all experiments, less than 1% of particles enter mixed layers deeper than 1000 m through convective events.

Text S3.

We begin by discussing the errors in the Lagrangian overturning streamfunction of *Döös et al.* [2008], which is formulated to be directly comparable to the residual overturning streamfunction (which they call the "Eulerian streamfunction"). In their Figures 4a and 4b, they find an upper cell of roughly 10 Sv for both the Lagrangian and Eulerian calculations. In their Figure 4c, they plot the difference (error) between the Lagrangian and Eulerian streamfunctions, which appears to be less than 2 Sv for most of the upper cell but between 2 Sv and 10 Sv in some localized places. The 4 Sv contouring of the plots makes it difficult to judge the skill of the Lagrangian calculation as there could potentially be up to 2 Sv (or about 20%) error everywhere in the upper cell. They attribute this error to the looping discontinuity, time sampling, and trajectory accuracy, acknowledging that there may be some additional unknown errors.

We now discuss these sources of error and others for our present study. While we did not explicitly test the impact of looping in our study, we note that *Thomas et al.* [2015] showed in a study of Northern Atlantic overturning that their Lagrangian calculations

were insensitive to the looping discontinuity. We acknowledge that even our experiments with 5-day averaged velocities are not using the online velocities and therefore likely have some error due to the time sampling (this is the same process by which we purposefully temporally degrade our velocity fields from 5-day averages to monthly averaged to remove eddy kinetic energy).

In addition to the sources of error discussed in *Döös et al.* [2008], there are a few potential sources of error specific to our Lagrangian method.

1) Although the Lagrangian experiments are run long enough to resolve the tails of the transit-time distributions, there may still be entire modes of the transit-time distribution that are unresolved (see discussion of multi-modal distributions in Supplemental Text S4); this hypothesis is particularly relevant for the pathways that exist in the eddying models but do not exist in CM2-1deg-5day, possibly because the timescales for the particles in CM2-1deg-5day are longer than the integration time of 500 years. We do not have any reason expect this to be the case but can not rule it out from our results alone.

2) Many particles that are released with an initially southward velocity will nevertheless travel north of 30°S at some point before they reach the upper ocean; in all cases, these particles are omitted from our analysis because our domain ends one grid cell north of 30°S. Had these particles been included in our analysis, some small subset of particles may have spent time north of 30°S after their release and before traveling south to upwell into the upper layers of the Southern Ocean. Despite the fact that these particles are released with an initial southward velocity and eventually reach the upper ocean south of 30° S, we justify omitting them because their southward transport will already be counted by the

new particles released at the locations and times that the original particles last crossed south of 30°S. For yet a smaller subset of these particles which spend only the first 30 days of their journey north of 30°S, we argue these particles will not be counted by a future particle release and thus should be included in estimates of LUT. Because our domains end one grid cell north of 30°S, we are unable to consistently resolve trajectories in this buffer region (which depends strongly on model resolution) to correct for this effect. In CM2-1deg-5day, our model with the largest buffer region (30°S to 29°S), we estimate a lower bound of 0.2 Sv of particles that are omitted. This estimate may increase as resolution increases and the large scale motions become more turbulent. We do not expect this source of error to be important here because our buffer zone is so small but note that in other models we have worked with where the buffer zone was 10° wide and the analysis included particles that spent time in the buffer zone, the error due to this double counting was as big as the signal itself!

3) Regridding the velocity field from its native B-grid to an A-grid is convenient for computing trajectories in CMS but complicates the representation of the no-normal flow boundary condition at topography; as a result, we find that some particles become trapped in corners of topography where flow is into the wall of the A-grid. We expect this to bias our LUT estimate low but note that many of these particles were initially released with small velocities very near bottom topography and thus both represent little overall transport (less than 10% of the total) and were anyways unlikely to be classified as upwelling Circumpolar Deep Water.

In a worst case estimate (where we take the high end of error from *Döös et al.* [2008] and add on the high end of our model-specific sources of error), we estimate an upper bound of 30% error on our estimate of LUT. It is unclear how these errors would affect the upwelling timescale, except that the particles trapped at topography and particles with timescales longer than the integration times may add to the slow tails of the distribution. Such long-timescale particles would likely not effect the mode of the TTD anyways, which we highlight as our primary timescale metric.

Text S4. We fit a three-parameter inverse Gaussian distribution separately to each of the six individual pathways in a given experiment by the least-squares method. The inverse Gaussian distribution is an analytical solution for the probability distribution of tracer age in a steady uniform flow with constant diffusivity and has been previously used to describe tracer-derived TTD [*Waugh et al.,* 2003]. A constant scaling parameter is multiplied to the inverse Gaussian function to allow the integral of the analytical TTD to be greater than one, thus accounting for additional particle-transport that may not be captured within the integration time limits of the experiment. The scaled inverse Gaussian, $f(t)$, is defined as follows:

$$f(t) = C\sqrt{\frac{\Gamma^3}{4\pi\Delta^2 t^3}}\exp\Big(\frac{-\Gamma(t-\Gamma)^2}{4\Delta^2 t}\Big) \tag{1}$$

where t is the transit-time [*Waugh et al.,* 2003] and the three parameters are: C, the multiplicative scaling parameter that accounts for particle-transport that has not yet upwelled; Γ, the mean transit-time; and Δ, the width of the analytical TTD. The analytical TTD for each pathway is then scaled by the corresponding particle-transport such that

its integral from 0 years to infinity is an estimate of the particle-transport expected to reach the upper ocean from 30°S, independent of the Lagrangian experiment time limit (Supplementary Fig. S5a-d). This extrapolation allows us to extend the inverse Gaussian curves analytically to account for the $< 3\%$ additional particle-transport that is expected to upwell after the integration time of the experiments. While this approach does not significantly change the results of this paper because most of the particle-transport is resolved, this approach may be useful to reconstruct a TTD when only part of the TTD is resolved from data. Studies on observational tracers and modeled Lagrangian trajectories provide examples of bimodal TTDs that fit the inverse Gaussian form poorly [*Haine et al., 2002; Iudicone et al.,* 2008]. In order to determine an accurate analytical fit to a potentially multimodal total TTD, we sum the transport-scaled analytical TTDs of the six individual pathways (Supplementary Fig. S5e).

Movie S1. The 30 year time-evolution of Lagrangian trajectories of particle-transport between a release depth of 2000 m at 30°S and the upper layers of the Southern Ocean. The trajectories selected for the movie correspond to the subset of particle-transport released on January 15th of the model year 183 and on the model depth level closest to 2000 m. Vertically exaggerated model bathymetry is shown in blue and model land elevation (1/3 vertical scale of ocean) is shown in green-brown-white.

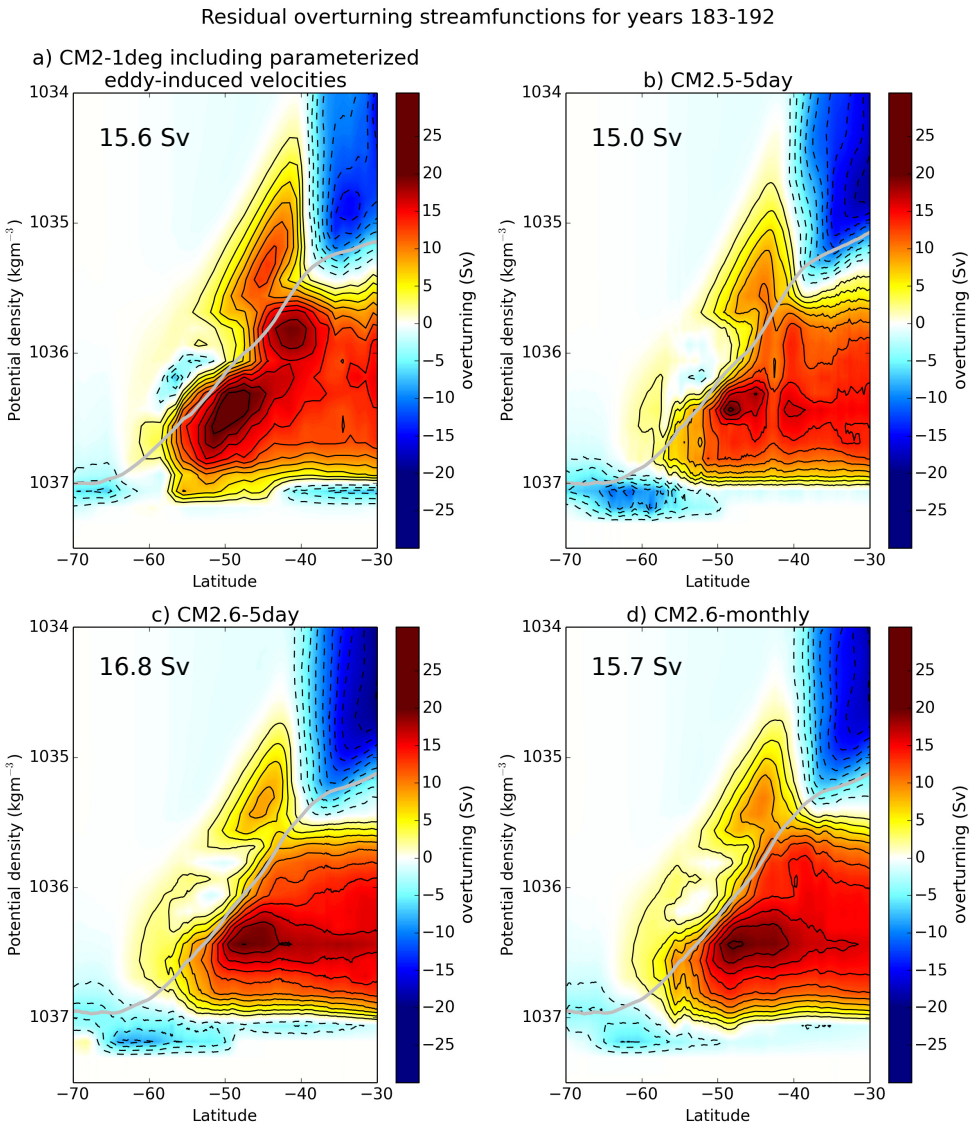

Figure S1. The residual overturning streamfunctions poleward of 30°S averaged over release years 183-192 in a) CM2-1deg-5day (1°, including parameterized eddy-induced transports), b) CM2.5-5day (0.25°), c) CM2.6-5day (0.1°), d) CM2.6-monthly (0.1°, temporally degraded velocities). Red colors denote clockwise circulation (2 Sv solid black contour lines) and blue colors denote counter-clockwise circulation (2 Sv dashed black contour lines). Overturning transports are binned online into potential density layers referenced to 2000 m. The thick grey line shows the zonally-averaged density of the 300m depth surface as a function of latitude. In the top left is the maximum value of the residual overturning streamfunction at 30S.

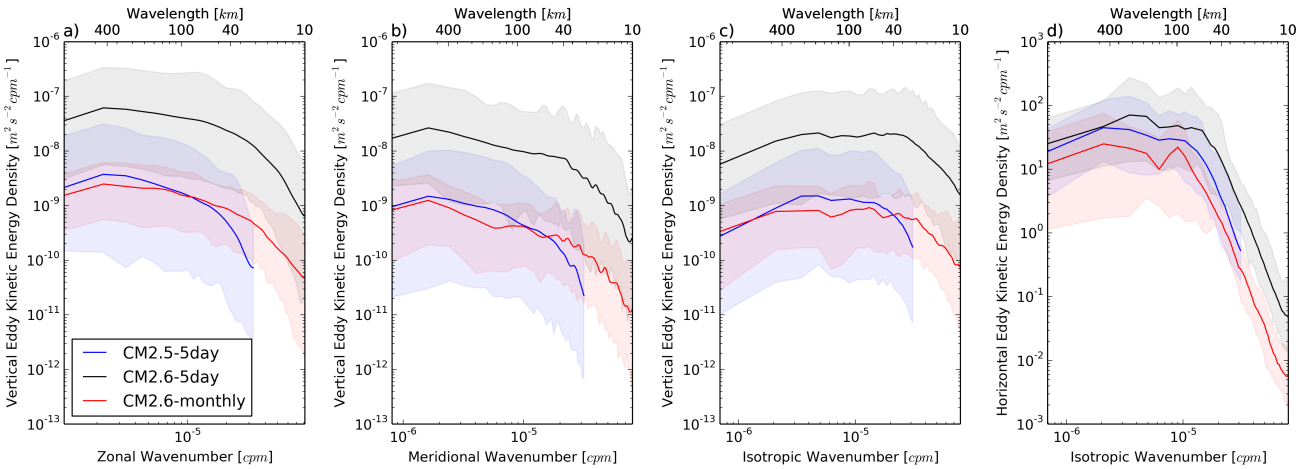

Figure S2. Mean (solid lines) and spread (shading) vertical eddy kinetic energy wavenumber spectra in CM2.5-5day (blue), CM2.6-5day (black), CM2.6-monthly (red) calculated from all snapshots in the first year of velocity output as a function of (a) zonal, (b) meridional, and (c) isotropic wavenumber in cycles per meter. (d) Same but for isotropic wavenumber spectrum of horizontal eddy kinetic energy. Ticks designate tenths of the next largest integer power of 10 wavenumber. Wavelengths in km are given along the top axis.

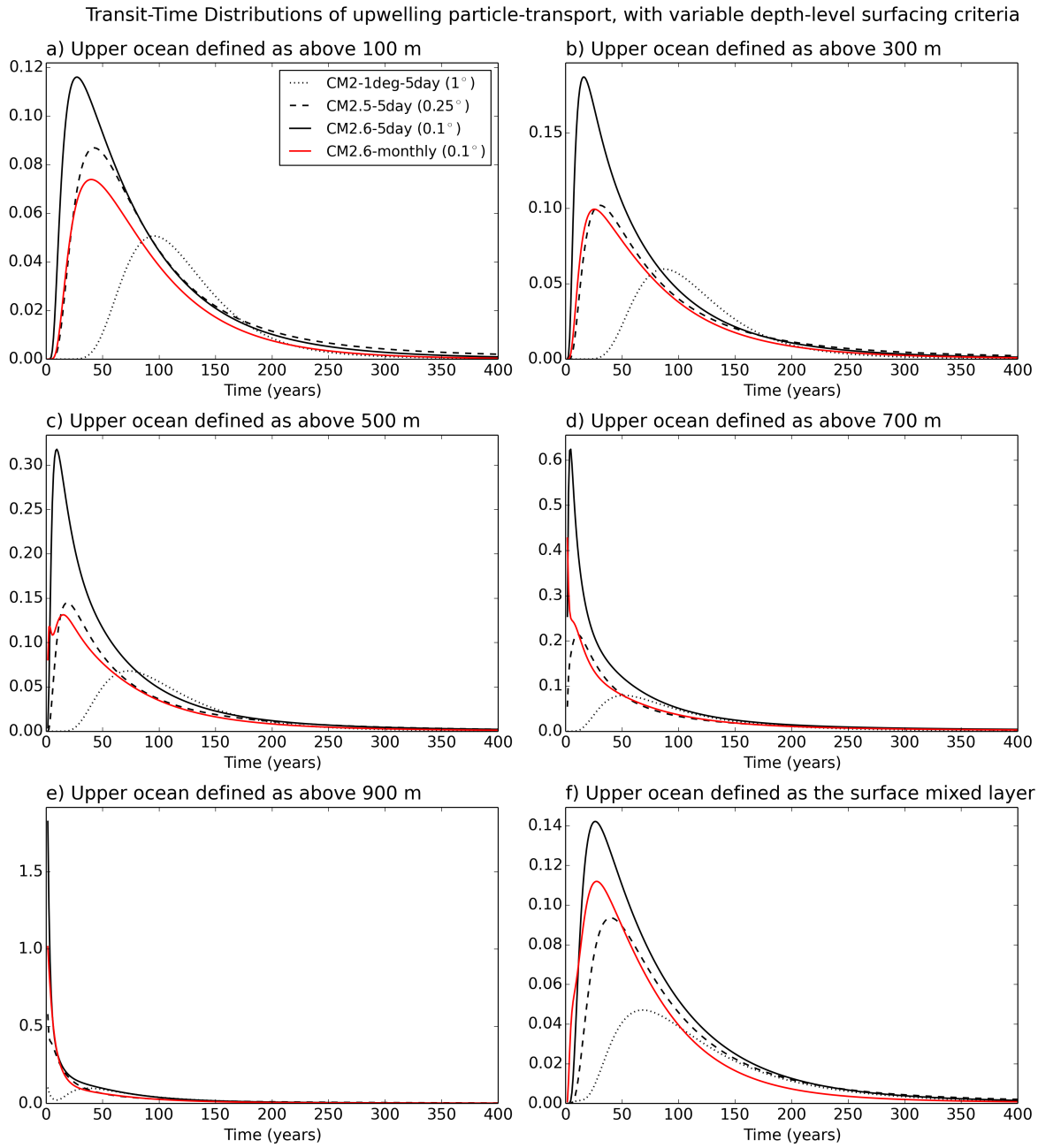

Figure S3. As in Figure 2a (upwelling TTD with upper ocean defined as the ocean above 300 m depth), but using the following different definitions of the upper ocean: a) shallower than 100m depth, b) shallower than 300 m depth, c) shallower than 500 m depth, d) shallower than 700 m depth, e) shallower than 900m depth, f) within the surface mixed layer.

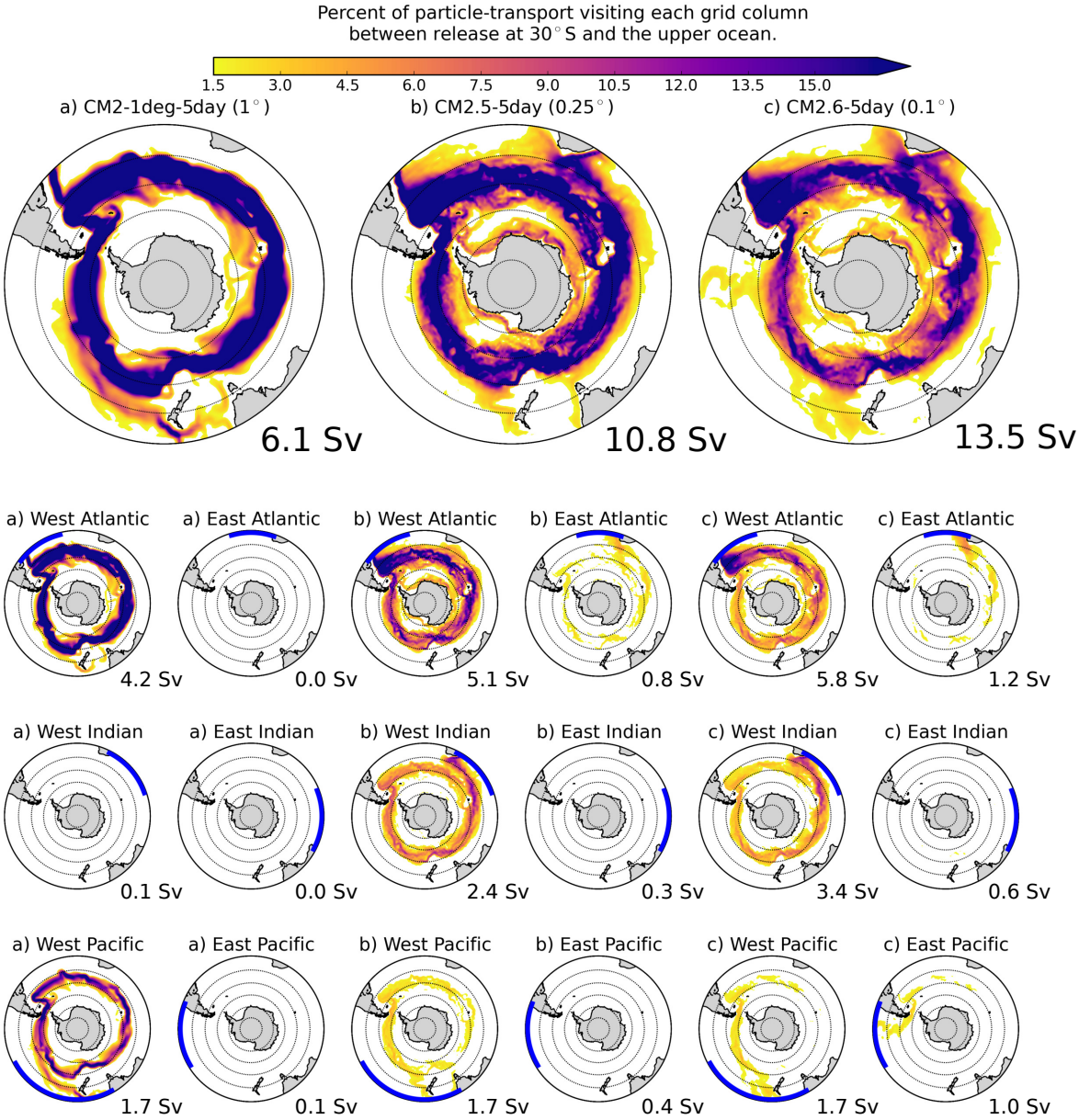

Figure S4. The three larger plots above are identical to the three panels of Figure 1. The plots below show decompositions of the above three plots by release section at 30°S (blue line).

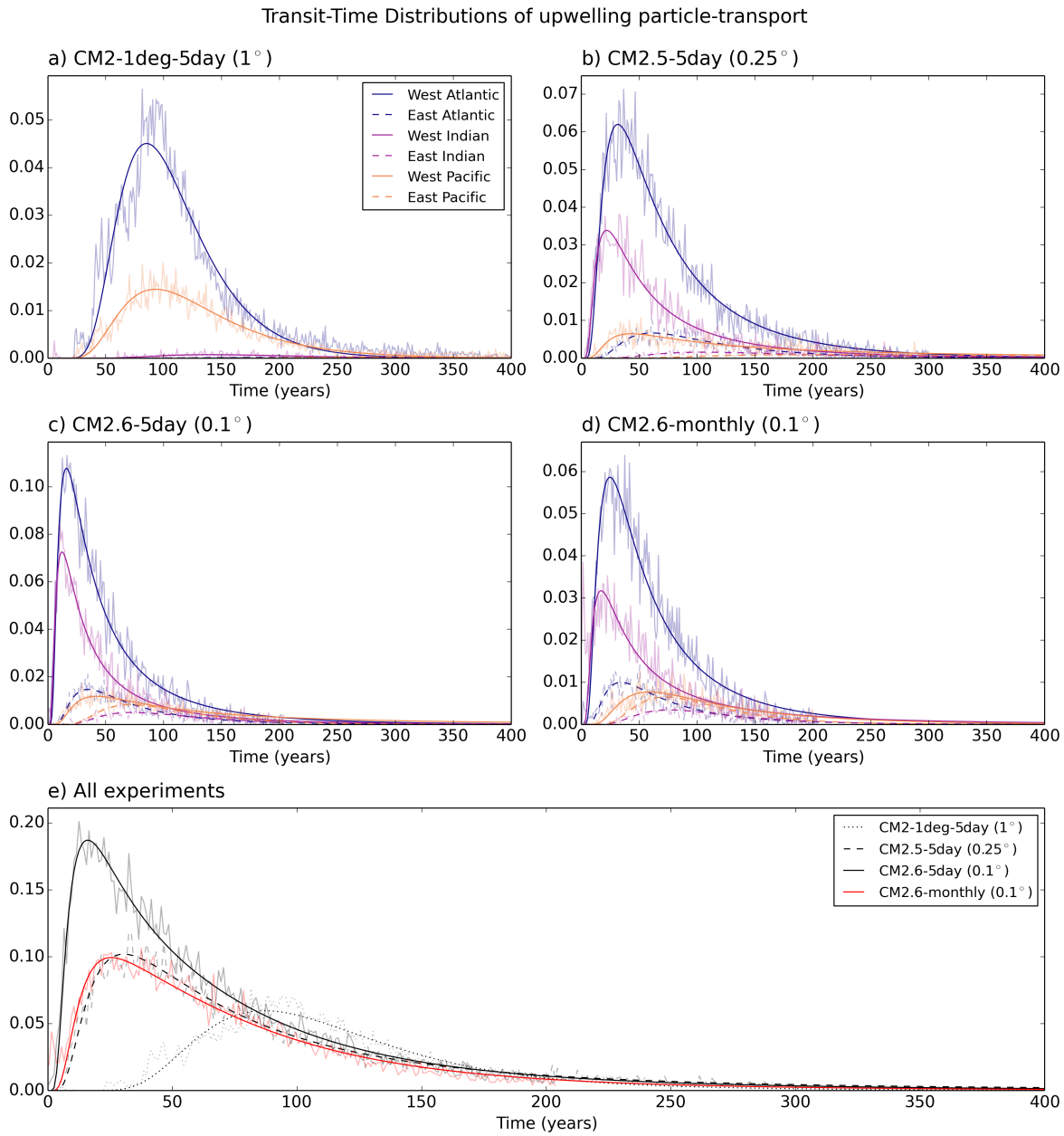

Figure S5. a), b), c), and d) are decompositions of Figure 2a into the six individual TTDs: a western and eastern TTD for each of the major ocean basins: the Atlantic Ocean, the Indian Ocean, and the Pacific Ocean. The analytical inverse Gaussian TTD fits are plotted with slightly transparent yearly-binned raw data overlaid. e) shows the sum of the raw data (slightly transparent) and sums of the inverse Gaussian fits (opaque) in a), b), c), and d). The opaque curves in e) are those reproduced in Figure 2a of the main text.

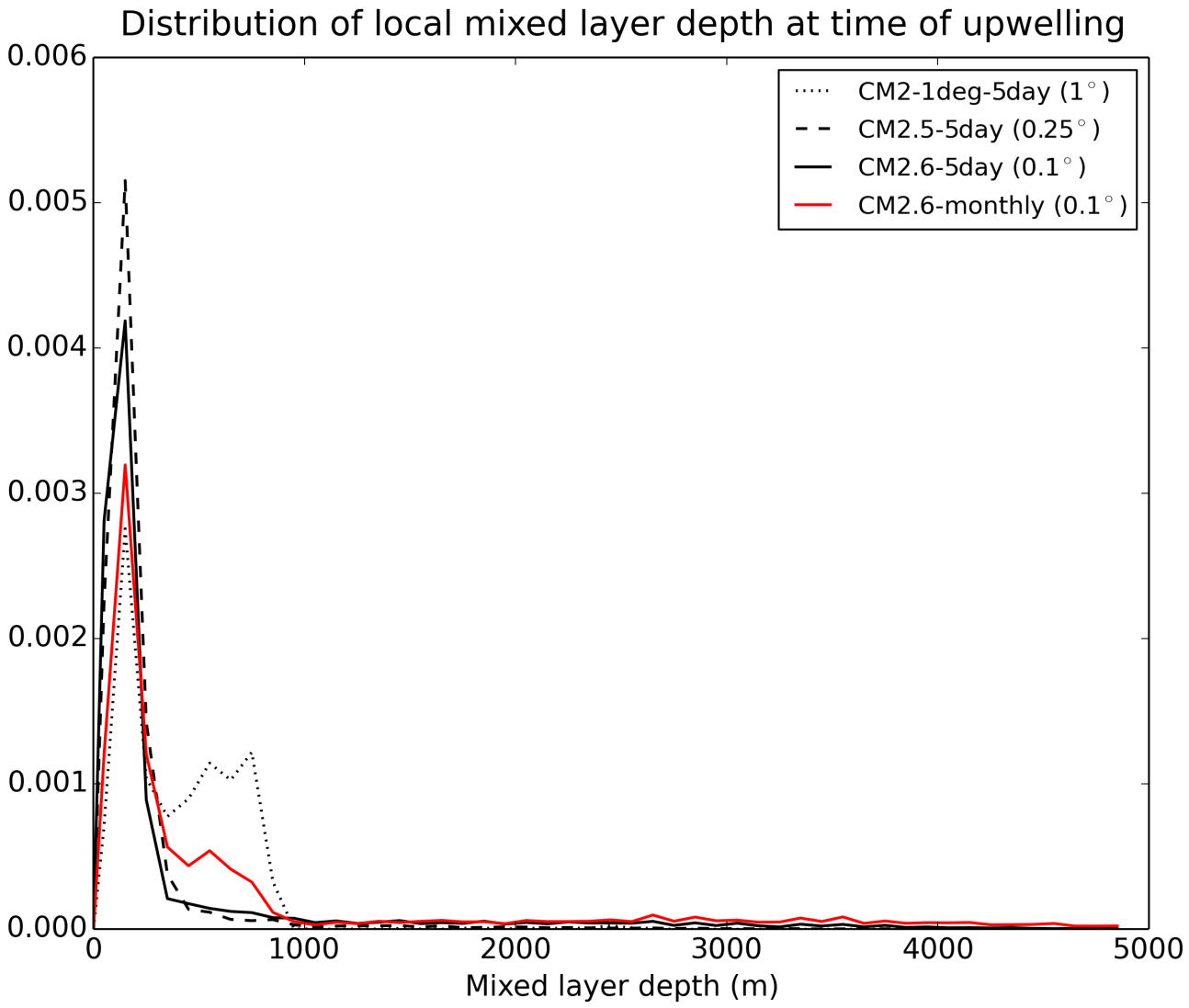

Figure S6. Percent of particle-transport upwelling into the surface mixed layer per year in experiments a) CM2-1deg-5day (1°), b) CM2.5-5day (0.25°), c) CM2.6-5day (0.1°), and d) CM2.6-monthly (0.1°, temporally degraded). We note in particular that upwelling into 500-1000 m deep mixed layers mostly corresponds to lateral advection into mid-latitude deep mixed layers (see also Supplementary Fig. 7), which suggests fixed depth cut-offs are a more useful criteria than the spatially-varying depth of the mixed layer for determining interior upwelling timescales.

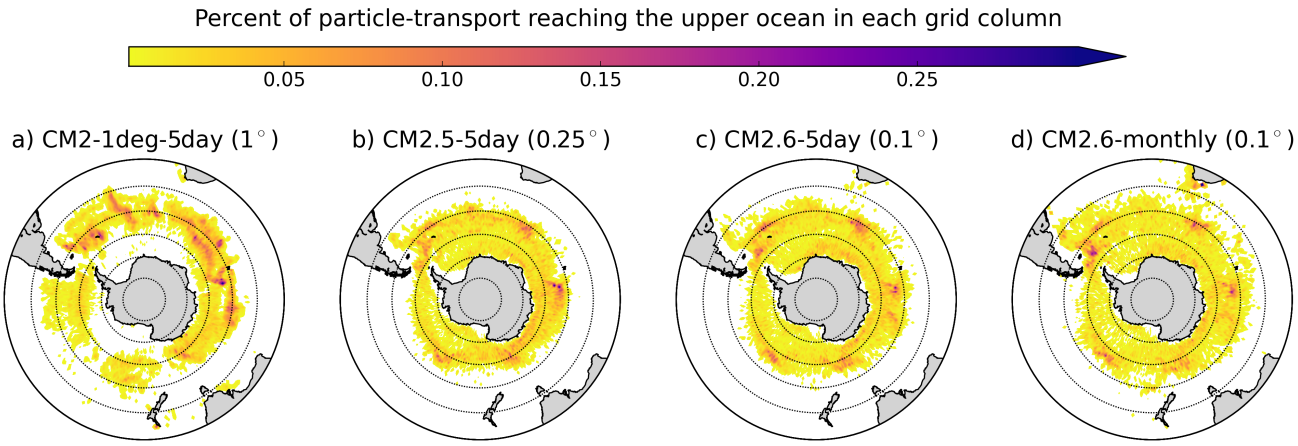

Figure S7. Percent of particle-transport upwelling into the surface mixed layer in each 1° by 1° grid column in experiments a) CM2-1deg-5day (1°), b) CM2.5-5day (0.25°), c) CM2.6-5day (0.1°), and d) CM2.6-monthly (0.1°, temporally degraded). We note in particular that the mid-latitude upwelling in a) and d) mostly reflect lateral advection into deep mixed layers, which suggests fixed depth cut-offs are a more useful criteria than the spatially-varying depth of the mixed layer for determining interior upwelling timescales.